# Multimodal hard X-ray imaging of a mammography phantom at a compact synchrotron light source

Simone Schleede,[a]* Martin Bech,[a,b] Klaus Achterhold,[a] Guillaume Potdevin,[a] Martin Gifford,[c] Rod Loewen,[c] Cecile Limborg,[d]‡ Ronald Ruth[d]¶ and Franz Pfeiffer[a]

[a]Technische Universität München, James-Franck-Strasse 1, D-85748 Garching, Germany, [b]Lund University, Barngatan 2:1, 22185 Lund, Sweden, [c]Lyncean Technologies Inc., 370 Portage Avenue, Palo Alto, CA 94306, USA, and [d]SLAC National Accelerator Laboratory, 2575 Sand Hill Road, Menlo Park, CA 94025, USA. E-mail: schleede@tum.de

The Compact Light Source is a miniature synchrotron producing X-rays at the interaction point of a counter-propagating laser pulse and electron bunch through the process of inverse Compton scattering. The small transverse size of the luminous region yields a highly coherent beam with an angular divergence of a few milliradians. The intrinsic monochromaticity and coherence of the produced X-rays can be exploited in high-sensitivity differential phase-contrast imaging with a grating-based interferometer. Here, the first multimodal X-ray imaging experiments at the Compact Light Source at a clinically compatible X-ray energy of 21 keV are reported. Dose-compatible measurements of a mammography phantom clearly demonstrate an increase in contrast attainable through differential phase and dark-field imaging over conventional attenuation-based projections.

Keywords: medical X-ray imaging; phase contrast; inverse Compton X-rays.

## 1. Introduction

Image quality in conventional absorption-contrast X-ray mammography is limited by the small differences in the mass absorption coefficients of soft tissues and the maximum dose that may be received by a patient in mammography screenings (Arfelli et al., 2000; Pisano et al., 2000). As elements with a low atomic number $Z$ produce very weak X-ray absorption but considerably higher phase signal, phase-contrast imaging techniques have the potential to reduce radiation dose and increase sensitivity at the same time. Different imaging techniques have been developed to detect the phase change of the incoming wavefront caused by the sample. As both phase propagation effects as well as analyzer-based imaging methods yield the best results with high monochromatic flux and spatial coherence, benchmarking experiments in multimodal mammography imaging have been carried out at synchrotron sources (Momose, 2003; Fitzgerald, 2000). The use of phase propagation measurements proved better at detecting tumors in phase-contrast images compared with conventional absorption contrast (Arfelli et al., 2000; Olivo et al., 2009). First in vivo mammographic examinations on humans using

conventional absorption contrast have been carried out with X-rays from the ELETTRA synchrotron source (Castelli et al., 2007). Additionally, dark-field imaging of a mammography phantom demonstrated higher detail visibility compared with images from a conventional X-ray tube source (Ando et al., 2005). However, the large size of synchrotron radiation facilities combined with their costs raises doubts on the feasibility of applying these methods to a large number of patients in mammography screening programs. A compact Compton-based synchrotron source therefore presents an alternative, as it meets the criteria of clinical compatibility and still provides X-rays of high flux, narrow bandwidth and spatial coherence. Combined with a grating-based interferometer (Momose et al., 2003; Weitkamp et al., 2005; Pfeiffer et al., 2007, 2008), the set-up can be used for high-sensitivity phase-contrast, dark-field and absorption imaging. In this paper we will present first multimodal imaging results of a mammographic accreditation phantom at the Compact Light Source, and experimentally demonstrate that the three contrast modalities with complementary information yield an increased detail visibility. All measurements have been made at a clinically compatible X-ray energy of 21 keV.

## 2. The Compact Light Source (CLS)

The CLS is a laboratory-scale synchrotron X-ray source, commercially developed and manufactured by Lyncean

---

‡ Dr Cecile Limborg's contributions to this publication were as an employee of Lyncean Technologies Inc., and were not part of her present Stanford University duties or responsibilities.
¶ Professor Ronald Ruth's contributions to this publication were as a paid consultant of Lyncean Technologies Inc., and were not part of his Stanford University duties or responsibilities.

doi:10.1107/S0909049512017682 **525**
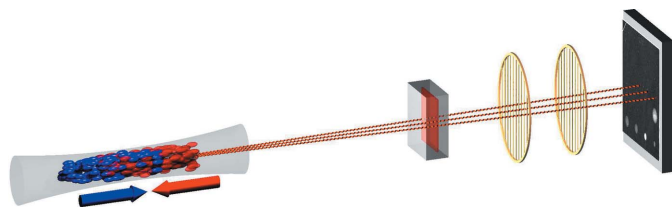
**Figure 1**
The Compact Light Source consists of an electron storage ring and a laser cavity. At the interaction point of the counter-propagating electron bunch (blue) and laser pulse (red), hard X-rays are produced in the process of inverse Compton scattering. The X-rays, which are emitted in a cone, shine onto the sample. The grating interferometer consists of two gratings and a PILATUS detector.

Technologies. A radio-frequency electron gun and a laser photocathode produce single electron bunches, which are accelerated to an energy in the range 20–45 MeV in the linear electron accelerator section. The bunch is stored at this energy in a miniature storage ring with a circumference of a few meters. A high finesse bowtie enhancement cavity is located at one of the straight sections of the storage ring and is resonantly driven by an infrared laser (Bech *et al.*, 2009). At the interaction point (sketched in Fig. 1) the laser and the electron bunch are tightly focused and pass through each other on each revolution of the electron bunch and each cycle of the laser pulse. Through the process of inverse Compton scattering, pulses of X-rays are produced on each revolution (Huang & Ruth, 1998). Let $\lambda_L$ and $\gamma$ denote laser wavelength and electron energy given in units of rest mass, respectively. The emitted spectrum is similar to that of a long magnetic undulator with the fundamental wavelength of the laser undulator being $\lambda_L/4\gamma^2$ (Loewen, 2003). As the laser wavelength used at the CLS is $\lambda_L \simeq 1$ μm, the electron energy needed to produce X-rays in the angstrom range is about two orders of magnitude lower than at large-scale synchrotron facilities. As a result the CLS storage ring can be scaled down to a few meters in circumference, making it feasible for use in a conventional laboratory or clinical environment. Tight focusing of both the electron bunch and the infrared laser results in high flux and a small source size of less than 50 μm × 50 μm r.m.s. This constitutes a considerable advantage compared with conventional mammography where a compromise between motion

blurring and geometrical blurring associated with large X-ray tube focal spot sizes has to be found. Microfocus X-ray tubes are limited in flux owing to the heat load on the target material and thus lead to an increase in overall exposure time, whereas the CLS offers both high flux and a small source size at the same time (Funke *et al.*, 1998; Koutalonis *et al.*, 2008). Furthermore, the high degree of spatial coherence can be exploited in the straightforward use of refraction-based imaging techniques. The intrinsic energy bandwidth of $\Delta E/E_{peak} = 3\%$ allows for monochromatic mammography which has proven to yield better results compared with polychromatic radiation (Moeckli *et al.*, 2000; Lawaczeck *et al.*, 2005). The angular divergence of about 4 mrad is larger than at conventional synchrotron sources and provides a circular field of view of 6.4 cm at a distance of 16 m from the source, which can be utilized to measure large biological samples.

## 3. Experiment

A grating interferometer was placed 16 m from the source. The $\pi/2$ phase shift grating $G_1$ with 5.31 μm pitch and an absorption grating $G_2$ with 5.4 μm pitch were used at the first fractional Talbot distance. The CLS was operated at a clinically compatible X-ray energy of $E_{peak} = 21$ keV ($\lambda_{peak} = 0.59$ Å), with a full energy spread of $\Delta E/E_{peak} = 3\%$. Each dataset consists of a phase-stepping scan of $G_2$ with respect to $G_1$ over one grating period using 32 steps. The exposure time for each phase step was 5 s resulting in a total exposure time of 160 s. All images were recorded using a PILATUS detector with square pixels of size 172 μm × 172 μm. From the flatfield images an average flux of $9.76 \times 10^5$ photons mm$^{-2}$ s$^{-1}$ has been estimated taking into account the detector efficiency, the absorption of the two gratings and surrounding air. The mammographic accreditation phantom (Gammex Model 156) approximates 4.2 cm of compressed breast. It is made up of a wax block containing 16 test objects (Fig. 2) including different sizes of nylon fibers which simulate fibrous structures, tumor-like masses and groups of simulated microcalcifications. The mean glandular dose was calculated by assuming a 50% glandular and 50% adipose by weight breast tissue composition with an outer 0.5 cm-thick adipose layer. The mean glandular dose of 8.75 mGy used to record the full dataset (as
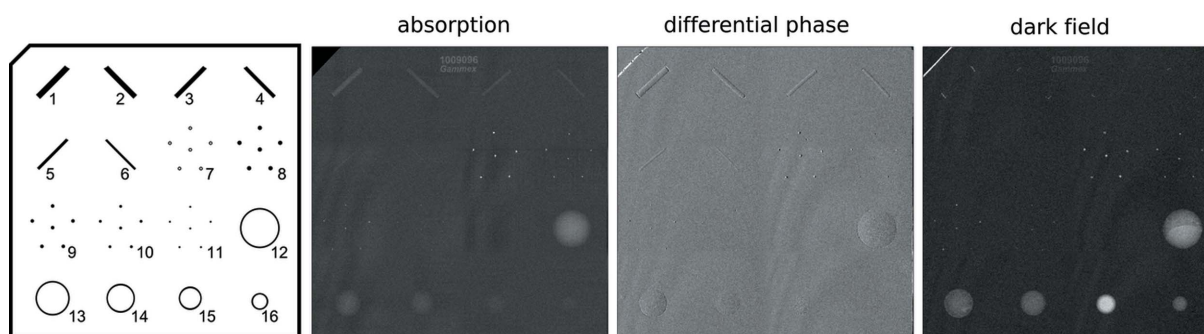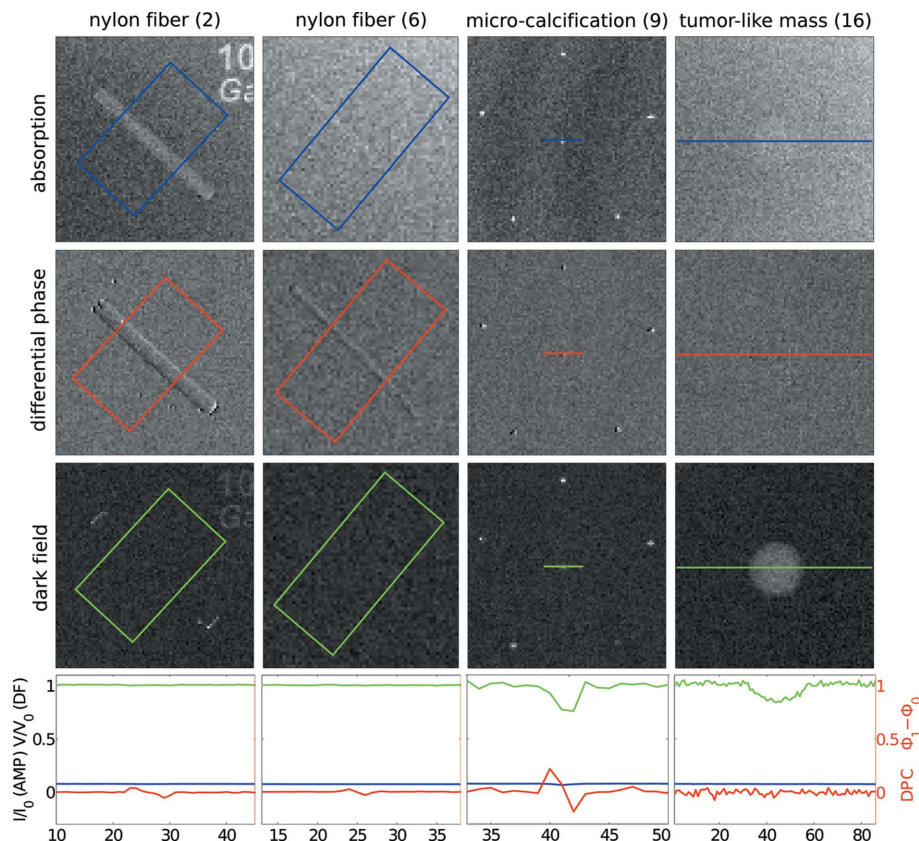


**Figure 2**
Location of the test objects in the mammographic accreditation phantom and their position in relation to the notched corner of the wax block. Absorption, differential phase-contrast and the dark-field images are shown. Each image displays six images stitched together, resulting in a total field of view of 8.0 cm × 8.1 cm.

displayed in Fig. 2) has been calculated according to the method of Arfelli *et al.* (1998) using the tissue X-ray properties as given by Dance *et al.* (1999). The dose of this proof-of-principle experiment is higher than the upper dose limit for single-view mammography of 3 mGy (NCRP, 2004). It can be significantly reduced through thinning of the grating wafers (which currently comprise 1 mm of silicon) and an improved detector efficiency at 21 keV. Dose-compatible results are shown in Fig. 4, where a reduced number of phase steps and thus shorter overall exposure times (20 s) have been used. The combination of more efficient X-ray detection after penetration of the sample and an expected increase in overall flux from the X-ray source will further reduce the exposure time down to clinically compatible values.

## 4. Results

Each individual dataset consists of 32 phase steps over one grating period. The flatfield image serves as a reference frame to account for local changes in intensity, curvature and coherence of the X-ray beam. The effect of the sample on the wavefront is then calculated using Fourier analysis, resulting
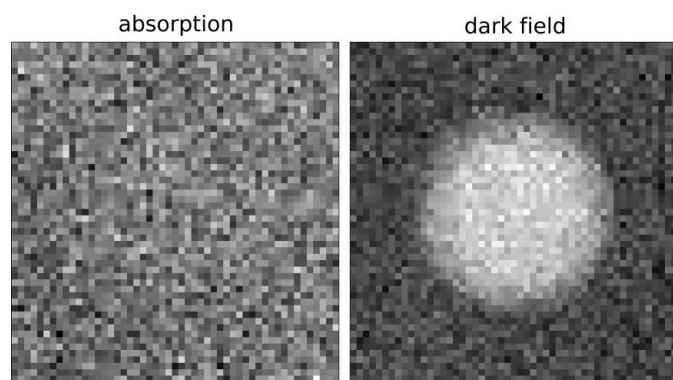


**Figure 3**
Test objects 2 (1.12 mm nylon fiber), 6 (0.40 mm nylon fiber), 9 (0.32 mm simulated micro-calcification) and 16 (0.25 mm-thick tumor-like mass) of the mammographic accreditation phantom (Fig. 2) are shown in conventional absorption, differential phase-contrast and dark-field contrast. Color bars in the images indicate sections where line plots of the contrast signal have been extracted. Absorption $I/I_0$, differential-phase $\Phi - \Phi_0$ and dark-field signal $V/V_0$ are obtained from a Fourier analysis of the phase-stepping scan as described by Pfeiffer *et al.* (2009).

in three different contrast modalities (Pfeiffer *et al.*, 2009): standard absorption, phase-contrast and dark-field images. Next to the sketch of the phantom geometry (Fig. 2) the mammography phantom is displayed in all three contrast modalities. Image contrast is adjusted to give maximum detail readability. Six projections have been stitched together to cover the entire mammography phantom. It is important to note that the field of view is limited by the active area of the PILATUS detector of 8.38 cm × 3.35 cm.

A comparison of the detectability of the test objects in the different contrast modalities demonstrates that the phase and the dark-field image provide additional information to the conventional absorption image. The small nylon fibers (test object 5 and 6 in Fig. 2) are not visible in the absorption and dark-field image, but are clearly visible in the phase-contrast image. All tumor-like masses, test objects 12, 13, 14, 15 and 16, appear more visible in the dark-field image compared with the absorption image. The smallest tumor-like mass in the phantom, test object 16, is not visible in the absorption-contrast image and is thus only detectable by use of the dark-field image. The large difference in scattering strength from tumor-like masses 15 compared with 14 indicates a variation in material homogeneity not obvious from the absorption image.

Fig. 3 shows imaging results of selected test objects of the mammographic accreditation phantom including line plots of absorption, differential phase and dark-field values that can be used to quantitatively compare the different contrast modalities. The line plots corresponding to the nylon fibers were calculated by integrating the pixel values along the direction of the nylon fiber over the region indicated by colored rectangles. Both nylon fibers (test objects 2 and 6) are significantly more visible in the differential phase-contrast image. In the case of the tumor-like mass (test object 16) and the micro-calcifications (test object 9), the plot displays one line through the original image indicated by a color bar.

Simulated micro-calcifications and tumor-like masses appear more visible in the phase-contrast and the dark-field image. The line plots of the absorption signal (blue) and dark-field signal (green) demonstrate a significant increase in contrast-to-noise ratio (CNR) in the dark-field image.

Fig. 4 shows absorption and dark-field imaging results of test object 15 (0.50 mm-thick tumor-like mass) recorded by using a mean glandular dose of 1.09 mGy (four phase steps). The reduction in dose has been achieved by processing only four of the 32 recorded phase steps. As the exposure time of each phase step remained constant throughout the experi-

**Figure 4**
Dose-compatible absorption and dark-field contrast image of test object 15 (0.50 mm-thick tumor-like mass). The tumor-like mass is clearly depicted in the dark-field image. A combination of the two contrast modalities leads to better tumor detectability using less than the conventional two-view mammography clinical dose (Boone *et al.*, 2001). Both images have been scaled to their minimum and maximum pixel values.

ment, this approach results in a reduction of dose by a factor of eight. A comparison of the tumor-like mass in absorption and dark-field contrast demonstrates superior tumor detectability in the dark-field image using less than the single-view mammography clinical dose (NCRP, 2004). A dedicated CNR analysis of the absorption and dark-field signal of test object 15 is displayed in Table 1. The contrast-to-noise values have been calculated in an area of $14 \times 11$ pixels in the tumor-like mass and the surrounding material pixels, respectively,

$$\text{CNR} = |S_a - S_b|/(\sigma_a^2 + \sigma_b^2)^{1/2}, \qquad (1)$$

where $S_a$ and $S_b$ represent the mean value of the signal in region $a$ and $b$, respectively, and $\sigma_a$ and $\sigma_b$ correspond to the standard deviation of the respective signals. A superior detectability of the test object in the lowest-dose (four phase steps) dark-field image compared with the 32-phase-steps (maximum dose in the experiment) absorption-contrast image has been achieved. This result indicates the potential for further reduction in dose through the use of multimodal imaging techniques without a decrease in image quality and tumor detectability. Furthermore, it should be noted here that all other tumor-like masses in the phantom show a less distinct difference in the CNR of the dark-field and absorption signal, which has to be attributed to different scattering strengths and thus differing microstructure of the materials used to create the tumor-like masses in the phantom. This implies that there is a need for dedicated phase-contrast and dark-field mammography phantoms which allow for a detailed comparison of breast imaging techniques that exploit refraction and scattering effects of X-rays in tissue.

## 5. Conclusion

The standard mammographic accreditation phantom (Gammex 156) has been measured in a first proof-of-principle experiment at a compact synchrotron light source using a grating-based interferometer. We achieved a better detect-

**Table 1**
Contrast-to-noise-ratio (CNR) of selected regions of the absorption and dark-field images of a tumor-like mass (test object 15).

As the exposure time of each phase step remained unchanged during the experiment, a reduction in number of processed phase steps results in a lower dose to the phantom. Note that the low contrast-to-noise-ratio ($\text{CNR}_{amp} < 1$) of the absorption signal corresponds to a noise level that is higher than the difference in mean pixel values and therefore does not allow for tissue discrimination in the image.

| Number of phase steps | $\text{CNR}_{amp}$ | $\text{CNR}_{DCI}$ |
|---|---|---|
| 4 | 0.1 | 4.7 |
| 8 | 0.1 | 6.5 |
| 16 | 0.1 | 9.2 |
| 32 | 0.1 | 12.8 |

ability of all test objects by combining the complementary information of absorption, differential phase-contrast and dark-field images. By focusing on single test objects in the phantom, enhanced contrast of the differential phase-contrast and dark-field signal compared with the conventional absorption image has been demonstrated. Dose-compatible dark-field measurements with high CNR of tumor-like masses have been demonstrated. Future work will focus on comparing our results with radiographs taken at a conventional mammographic unit and further reducing the dose of these multimodal imaging experiments. We plan to achieve this by improving grating quality, experimental procedure and data processing. The results indicate the potential of improved tumor detectability in mammography screening programs. Experiments on fixated breast tissue are planned.

## References

Ando, M., Yamasaki, K., Toyofuku, F., Sugiyama, H., Ohbayashi, C., Li, G., Pan, L., Jiang, X., Pattanasiriwisawa, W., Shimao, D., Hashimoto, E., Kimura, T., Tsuneyoshi, M., Ueno, E., Tokumori, K., Maksimenko, A., Higashida, Y. & Hirano, M. (2005). *Jpn. J. Appl. Phys.* **44**, L528–L531.
Arfelli, F., Bonvicini, V., Bravin, A., Cantatore, G., Castelli, E., Dalla Palma, L., Di Michiel, M., Longo, R., Olivo, A., Pani, S., Pontoni, D., Poropat, P., Prest, M., Rashevsky, A., Tromba, G. & Vacchi, A. (1998). *Radiology*, **208**, 709–715.
Arfelli, F., Bonvicini, V., Bravin, A., Cantatore, G., Castelli, E., Palma, L. D., Michiel, M. D., Fabrizioli, M., Longo, R., Menk, R. H., Olivo, A., Pani, S., Pontoni, D., Poropat, P., Prest, M., Rashevsky, A., Ratti, M., Rigon, L., Tromba, G., Vacchi, A., Vallazza, E. & Zanconati, F. (2000). *Radiology*, **215**, 286–293.
Bech, M., Bunk, O., David, C., Ruth, R., Rifkin, J., Loewen, R., Feidenhans'l, R. & Pfeiffer, F. (2009). *J. Synchrotron Rad.* **16**, 43–47.

Boone, J. M., Nelson, T. R., Lindfors, K. K. & Seibert, J. A. (2001). *Radiology*, **658**, 657–667.

Castelli, E., Arfelli, F., Dreossi, D., Longo, R., Rokvic, T., Cova, M., Quaia, E., Tonutti, M., Zanconati, F. & Abrami, A. (2007). *Nucl. Instrum. Methods Phys. Res. A*, **572**, 237–240.

Dance, D. R., Skinner, C. L. & Carlsson, G. A. (1999). *Appl. Radiat. Isot.* **50**, 185–203.

Fitzgerald, R. (2000). *Phys. Today*, **53**, 23–26.

Funke, M., Breiter, N., Hermann, K., Oestmann, J. & Grabbe, E. (1998). *Eur. Radiol.* **8**, 386–390.

Huang, Z. & Ruth, R. D. (1998). *Phys. Rev. Lett.* **80**, 976–979.

Koutalonis, M., Delis, H., Spyrou, G., Costaridou, L., Tzanakos, G. & Panayiotakis, G. (2008). *Phys. Med. Biol.* **53**, 1369–1384.

Lawaczeck, R., Rein, V. & Deeg, W. (2005). *Nucl. Instrum. Methods Phys. Res. A*, **548**, 147–154.

Loewen, R. J. (2003). *A Compact Light Source: Design and Technical Feasibility Study of a Laser–Electron Storage Ring X-ray Source*, SLAC-Report-632, Stanford University, USA.

Moeckli, R., Verdun, F. R., Fiedler, S., Pachoud, M., Schnyder, P. & Valley, J. F. (2000). *Phys. Med. Biol.* **45**, 3509–3523.

Momose, A. (2003). *Opt. Express*, **11**, 2303–2314.

Momose, A., Kawamoto, S., Koyama, I., Hamaishi, Y., Takai, K. & Suzuki, Y. (2003). *Jpn. J. Appl. Phys.* **42**, L866–L868.

NCRP (2004). *A Guide to Mammography and Other Breast Imaging Procedures*, NCRP Report 149. National Council on Radiation Protection and Measurements, Bethesda, MD, USA.

Olivo, A., Rigon, L., Vinnicombe, S. J., Cheung, K. C., Ibison, M. & Speller, R. D. (2009). *Appl. Radiat. Isot.* **67**, 1033–1041.

Pfeiffer, F., Bech, M., Bunk, O., Donath, T., Henrich, B., Kraft, P. & David, C. (2009). *J. Appl. Phys.* **105**, 102006.

Pfeiffer, F., Bech, M., Bunk, O., Kraft, P., Eikenberry, E. F., Brönnimann, Ch, Grünzweig, C. & David, C. (2008). *Nat. Mater.* **7**, 134–137.

Pfeiffer, F., Bunk, O., David, C., Bech, M., Le Duc, G., Bravin, A. & Cloetens, P. (2007). *Phys. Med. Biol.* **52**, 6923–6930.

Pisano, E. D., Johnston, R. E., Chapman, D., Geradts, J., Iacocca, M. V., Livasy, C. A., Washburn, D. B., Sayers, D. E., Zhong, Z., Kiss, M. Z. & Thomlinson, W. C. (2000). *Radiology*, **214**, 895–901.

Weitkamp, T., Diaz, A., David, C., Pfeiffer, F., Stampanoni, M., Cloetens, P. & Ziegler, E. (2005). *Opt. Express*, **13**, 6296–6304.